

# Accurate cell counts in live mouse embryos using optical quadrature and differential interference contrast microscopy

William C. Warger II<sup>\*1</sup>, Judith A. Newmark<sup>2</sup>, Bing Zhao<sup>1</sup>, Carol M. Warner<sup>2</sup>, Charles A. DiMarzio<sup>1</sup>

<sup>1</sup>Department of Electrical and Computer Engineering,  
Northeastern University, 440 Dana Building, 360 Huntington Ave., Boston, MA 02115

<sup>2</sup>Department of Biology,  
Northeastern University, 134 Mugar Building, 360 Huntington Ave., Boston, MA 02115

## ABSTRACT

Present imaging techniques used in *in vitro* fertilization (IVF) clinics are unable to produce accurate cell counts in developing embryos past the eight-cell stage. We have developed a method that has produced accurate cell counts in live mouse embryos ranging from 13 – 25 cells by combining Differential Interference Contrast (DIC) and Optical Quadrature Microscopy. Optical Quadrature Microscopy is an interferometric imaging modality that measures the amplitude and phase of the signal beam that travels through the embryo. The phase is transformed into an image of optical path length difference, which is used to determine the maximum optical path length deviation of a single cell. DIC microscopy gives distinct cell boundaries for cells within the focal plane when other cells do not lie in the path to the objective. Fitting an ellipse to the boundary of a single cell in the DIC image and combining it with the maximum optical path length deviation of a single cell creates an ellipsoidal model cell of optical path length deviation. Subtracting the model cell from the Optical Quadrature image will either show the optical path length deviation of the culture medium or reveal another cell underneath. Once all the boundaries are used in the DIC image, the subtracted Optical Quadrature image is analyzed to determine the cell boundaries of the remaining cells. The final cell count is produced when no more cells can be subtracted. We have produced exact cell counts on 5 samples, which have been validated by Epi-Fluorescence images of Hoechst stained nuclei.

Keywords: Optical Quadrature Microscopy, Differential Interference Contrast, embryo viability, phase subtraction cell counting method, IVF, OQM, QTM

## 1. INTRODUCTION

In the United States one in six couples suffers from problems related to infertility. *In vitro* fertilization (IVF) procedures have been available to these couples for more than 25 years, however the clinics are only able to provide a successful pregnancy rate of 30-40% [1]. The reason for the low success rate is the inability to determine which embryos are viable and will lead to a successful pregnancy. As a result, clinicians transfer multiple embryos to increase the chances of including one viable embryo that will produce a successful pregnancy. This practice produces a 20-40% risk of multiple pregnancy, which leads to an increased risk of pregnancy complications, preterm delivery, low birth weight, congenital malformations, and infant death [2]-[9]. There is also an increased risk of neurological problems, especially cerebral palsy, in multiple-birth infants created by IVF [10]. For these reasons there is a world-wide effort towards single embryo transfer [11].

Human embryos that are cultured in IVF clinics are given a grade based on two major criteria: 1) the number of cells at specific time points during development and 2) the overall morphology [12]-[30]. Some of the morphological parameters that have been considered are symmetry, size, color, fragmentation, vacuoles, perivitelline space, position of pronuclei, and orientation of nucleoli, but none of these parameters can reliably determine embryo viability. There is agreement that the second criterion, embryo cell number, shows that faster developing embryos are more likely to give rise to a successful pregnancy than slower developing embryos as reviewed in [22] and [24]. However, current non-toxic microscopy techniques are unable to count the number of cells accurately past the eight-cell stage. This limitation is not

important for Day 3 transfers where embryos containing less than ten cells are returned to the uterine environment, but is important for blastocyst stage (Day 5) transfers. Blastocyst transfers are advantageous because the embryo does not reach the uterus, where it is transferred during IVF, until day 5 in a natural pregnancy [31]. As a result, the decision on embryo quality in blastocyst transfers is based on subjective morphological markers alone. Therefore, the creation of an instrument that can non-invasively count the number of cells during embryo development up to the blastocyst stage would help physicians make a more educated determination of embryo viability and potentially provide the means for successful single embryo transfer.

## 2. DIFFERENTIAL INTERFERENCE CONTRAST

Clinicians presently use DIC, or the similar Hoffman optics, to analyze the morphological characteristics of the embryo and to make their best determination of the number of cells between the oocyte and blastocyst stages. A DIC image of an embryo provides distinct cell boundaries for cells within the focal plane of the objective because the cell boundaries provide the greatest difference in optical path lengths between the two waves. However, as the embryos develop, the cells begin to overlap and obstruct the edges of cells under the top layer. Cell edges are visible under a single layer of overlapped cells providing the ability to count accurately up to two layers of four cells. Once the developing cells begin to form a third layer after the eight-cell stage the cell edges of the third layer cannot be seen, thus making accurate cell counts unattainable by using DIC microscopy.

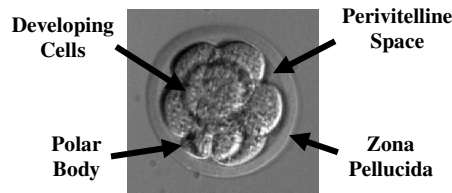


**Figure 1:** DIC image of a live mouse embryo. The zona pellucida surrounds the developing cells and polar body.

Figure 1 shows a DIC image of a typical eight-cell live mouse embryo. Each cell, or blastomere, divides into two cells with a combined volume approximately equal to the original cell before division. Thus the total volume of the embryo is unchanged during development. Two polar bodies are extruded during development and eventually degenerate within the embryo. The important characteristic of the polar body is that it is considerably smaller in size compared to the developing cells. The zona pellucida is a spherical shell that surrounds the cells and keeps them contained. The space that is between the cells and within the zona pellucida is called the perivitelline space. During imaging, it is assumed that the perivitelline space is filled with culture medium because the zona pellucida is porous.

## 3. OPTICAL QUADRATURE MICROSCOPY

Optical Quadrature Microscopy (OQM) non-invasively computes the amplitude and phase of an optically transparent sample [32]. A Mach-Zender interferometer configuration, seen in Figure 2, is used with a 633 nm HeNe laser for coherent illumination. Unpublished work in our laboratory has shown that  $0.66 \frac{mW}{cm^2}$  of 633 nm laser light was not toxic to 436 live mouse embryos over varying lengths of time thereby proving this method to be non-toxic to live mouse embryos [33].

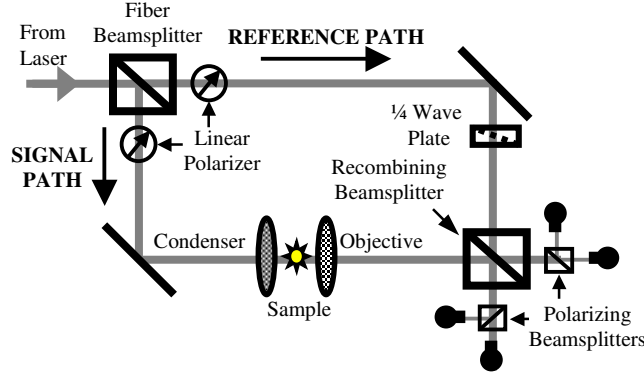


**Figure 2:** Mach-Zehnder configuration for Optical Quadrature Microscopy.

For OQM, the laser light is separated into the reference ( $E_{ref}$ ) and signal ( $E_{sig}$ ) paths by a fiber-coupled, non-polarizing beamsplitter and linearly polarized:

$$\vec{E}_{ref} = \frac{1}{\sqrt{2}} (E_R e^{j(\omega t + \phi)}) \cdot (\vec{x} + \vec{y}) \quad (1)$$

$$\vec{E}_{sig} = \frac{1}{\sqrt{2}} (E_S e^{j(\omega t + \phi)}) \cdot (\vec{x} + \vec{y}). \quad (2)$$

The phase of the laser output is described by  $\phi$  and the magnitude ( $E_L$ ) is derived from:

$$E_L = \sqrt{|\frac{1}{\sqrt{2}} E_L|^2 + |\frac{1}{\sqrt{2}} E_L|^2} = \sqrt{|\frac{1}{\sqrt{2}} E_R|^2 + |\frac{1}{\sqrt{2}} E_S|^2} \quad (3)$$

assuming a lossless beamsplitter. The reference path travels through a quarter wave plate to produce circular polarization while the signal path travels through the sample where a magnitude ( $A$ ) and phase ( $\alpha$ ) are introduced:

$$\vec{E}_{ref} = \frac{1}{\sqrt{2}} (E_R e^{j(\omega t + \phi)}) \cdot (\vec{x} + j\vec{y}) \quad (4)$$

$$\vec{E}_{sig} = \frac{1}{\sqrt{2}} (A E_S e^{j(\omega t + \phi + \alpha)}) \cdot (\vec{x} + \vec{y}). \quad (5)$$

The two paths are recombined with a 50/50 non-polarizing beamsplitter. Assuming the beamsplitter is lossless the total output power is given by:

$$\vec{E}_{sig}^2 + \vec{E}_{ref}^2 = |\frac{1}{\sqrt{2}} (\vec{E}_{sig} + \vec{E}_{ref})|^2 + |\frac{1}{\sqrt{2}} (\vec{E}_{sig} - \vec{E}_{ref})|^2. \quad (6)$$

The outputs from the two individual sides of the beamsplitter are arbitrarily chosen between either of the terms in (6) since the exact outputs cannot be determined. An optical quadrature image could be acquired from either output in (6) but both outputs of the recombining beamsplitter are used in a balanced detection configuration to increase the signal-to-noise ratio at the detectors. Polarizing beamsplitters separate the quadrature components of each output and the interferograms are captured with four CCD cameras. The signals captured for the first output in (6) are:

$$M_0 = |\frac{1}{\sqrt{2}} (\vec{E}_{sig} + \vec{E}_{ref}) \cdot \vec{x}|^2 \quad (7)$$

$$M_1 = |\frac{1}{\sqrt{2}} (\vec{E}_{sig} + \vec{E}_{ref}) \cdot \vec{y}|^2 \quad (8)$$

and the signals captured for the second output in (6) are:

$$M_2 = \left| \frac{1}{\sqrt{2}} (\vec{E}_{sig} - \vec{E}_{ref}) \cdot \vec{x} \right|^2 \quad (9)$$

$$M_3 = \left| \frac{1}{\sqrt{2}} (\vec{E}_{sig} - \vec{E}_{ref}) \cdot \vec{y} \right|^2 \quad (10)$$

where:

$$M_0 = \frac{1}{4} (A^2 E_S E_S^* + E_R E_R^* + A E_S E_R^* e^{j\alpha} + A E_R E_S^* e^{-j\alpha}) \quad (11)$$

$$M_1 = \frac{1}{4} (A^2 E_S E_S^* + E_R E_R^* - j A E_S E_R^* e^{j\alpha} + j A E_R E_S^* e^{-j\alpha}) \quad (12)$$

$$M_2 = \frac{1}{4} (A^2 E_S E_S^* + E_R E_R^* - A E_S E_R^* e^{j\alpha} - A E_R E_S^* e^{-j\alpha}) \quad (13)$$

$$M_3 = \frac{1}{4} (A^2 E_S E_S^* + E_R E_R^* + j A E_S E_R^* e^{j\alpha} - j A E_R E_S^* e^{-j\alpha}). \quad (14)$$

Ideally, balance mixing with the summation:

$$E_r = \sum_{n=0}^3 i^n M_n, \quad (15)$$

could reconstruct the resultant image, but fixed pattern noise caused by imperfections within the cameras and beamsplitters exists along the individual paths. Subtraction of the pure signal ( $S_n$ ), reference ( $R_n$ ), and dark detector voltage ( $D_n$ ) from the individual signals, (11) – (14), removes the fixed pattern noise and leads to the reconstruction:

$$E_r = \sum_{n=0}^3 i^n \frac{M_{nd} - R_{nd} - S_{nd}}{\sqrt{R_{nd}}} \quad (16)$$

where the subscript  $d$  signifies the subtraction of  $D_n$  from the component. Images are captured for  $S_n$ ,  $R_n$ , and  $D_n$  by blocking the signal and reference arms individually and simultaneously. The division by the square root of the pure reference normalizes the signals recorded by each of the cameras. A second image is reconstructed with the sample moved out of the field-of-view to create a blank image. Dividing the result of (16) by the blank image provides the complex magnitude and phase of the sample:

$$A e^{j\alpha} = \frac{E_r}{E_{r,blank}}. \quad (17)$$

The cell counting method presented in this paper only utilizes the phase ( $\alpha$ ) of the complex values in (17). The image of wrapped phase is unwrapped using a two-dimensional phase unwrapping algorithm to produce a quantitative image [34]. Finally, multiplying the unwrapped phase image by  $\frac{\lambda}{2\pi}$ , where  $\lambda$  is equal to 633 nm, provides an image of optical path length deviations (OPD image). The image is interpreted as optical path length deviation among various biological elements since ambiguities exist between the index of refraction and thickness of the object. An object with a certain index of refraction and thickness will appear the same as an object with half of the thickness and twice the index.

#### 4. EPI-FLUORESCENCE IMAGING

Fluorescence microscopy images the distribution of individual molecules by filtering out everything but specific wavelengths emitted (fluorescence) after excitation at a particular wavelength. For the studies that were conducted in

our laboratory, embryos were stained with Hoechst dye, which binds to the DNA within the nucleus of each cell and can be imaged with fluorescence microscopy. A cell count is completed visually by manually adjusting the focus. Counting the stained nuclei provides the ground truth to the number of cells within an embryo.

This method of cell counting would be ideal for clinicians since it is easy to use and offers a relatively fast measurement of the number of cells. However, the Hoechst stain permanently binds to the DNA of the nuclei and its use is therefore considered an invasive and potentially mutagenic procedure that is not permitted in a clinical setting. We only use this method to provide the ground truth for the number of cells in each embryo to prove the success of our cell counting procedure.

## 5. CELL COUNTING METHOD

The cell counting method presented in this paper utilizes the combination of Optical Quadrature and DIC images to count the cells within live mouse embryos. The DIC image, seen in Figure 3(a), shows distinct cell boundaries for the portions of cells that are not overlapped, and the OPD image, seen in Figure 3(b), can be interpreted as the relative thickness of the developing cells. The OPD image will first be used to determine the maximum optical path length deviation of a single cell, which is presently held constant for all cells subtracted in the process. Combining the maximum optical path length deviation of a single cell with a cell boundary created with the DIC image creates an ellipsoidal model cell of optical path length deviation. This model cell is subtracted from the OPD image revealing the optical path length deviation of either the culture medium or additional cells hidden under the subtracted cell. Model cells are subtracted from the OPD image until no cells remain and the cell count is complete.

The process begins by observing the DIC and OPD images side-by-side, as seen in Figure 3, in order to locate a cell that is along the perimeter of the developing cells, largely not overlapped by other cells, and approximately the same size as the other visible cells. Ideally a cell with no overlap should be chosen, but that is not possible in embryos beyond the eight-cell stage because every cell is overlapped by another cell.

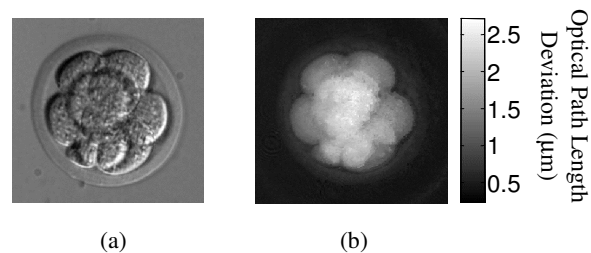


**Figure 3:** (a) DIC and (b) OQM images of a live mouse embryo. A cell is chosen with the least amount of overlap with other cells in the DIC image and with a uniform distribution of optical path length deviation in the OQM image to determine the optical path length deviation of a single cell.

Once the cell is chosen, the optical path length deviation is plotted for a line that traverses from the culture medium, outside the zona pellucida, through the center of the chosen cell, to an overlapped region of cells, as seen in Figure 4(b). The line must reach the region of overlapped cells to guarantee that the maximum optical path length deviation of the cell is visible in the plot. The plot of optical path length deviation, seen in Figure 4(a), is constant within the noise level of the image when the line is within the culture medium. The optical path length deviation begins to increase in a parabolic fashion as the line crosses the zona pellucida. The optical path length deviation reaches a local maximum point when the line reaches the inside edge of the zona pellucida since the cell is pressed against the zona pellucida. The plot of optical path length deviation increases again in a larger parabolic shape as the line crosses the non-overlapped portion of the chosen cell. The optical path length deviation increases again once the line reaches the overlapped portion of cells. Had the chosen cell not been overlapped by other cells, a full parabola would be seen in the plot of optical path length deviation.

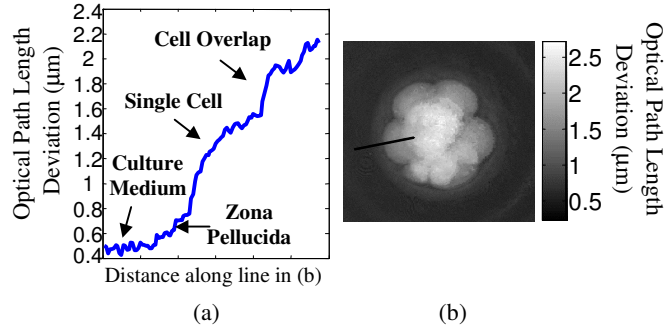


**Figure 4:** (a) Plot of optical path length deviation along the line drawn through the chosen cell on the OQM image in (b). The plot is labeled to relate the optical path length deviation to the biological origins.

Points are manually selected along the parabola corresponding to the optical path length deviation of a single cell. The first point represents the minimum optical path length deviation of a cell and is approximated as  $\frac{3}{4}$  of the optical path length deviation between the culture medium and the maximum value associated with the zona pellucida observed in the plot in Figure 4(a). This value was empirically determined because the zona pellucida is a shell of a certain thickness that surrounds the developing cells. That means there is some contribution of optical path length deviation from the top and bottom halves that is less than the maximum optical path length deviation of the inside edge of the zona that touches the cell in Figure 4(a) but more than the optical path length deviation of the culture medium. The remaining points are selected along the parabolic shape representing the optical path length deviation of a single cell to achieve a parabolic fit in Figure 4(a). The maximum optical path length deviation of a cell is recorded as the maximum point along the parabola created by the fit. The total optical path length deviation of a single cell is then defined as the difference between the maximum optical path length deviation of a cell and the approximated minimum optical path length deviation of a cell.

The OPD and DIC images are once again observed side-by-side to determine an elliptical boundary of a cell. Points are selected for the center of the ellipse, the minimum radius of the ellipse ( $a$ ), and the maximum radius of the ellipse ( $b$ ). An ellipse is created from these three points and displayed on the DIC and OPD images to confirm a proper fit as seen in Figure 5(a). Combining the radii of the ellipse with half of the total optical path length deviation of a single cell ( $c$ ) creates an ellipsoidal model cell of optical path length deviation seen in Figure 5(b).

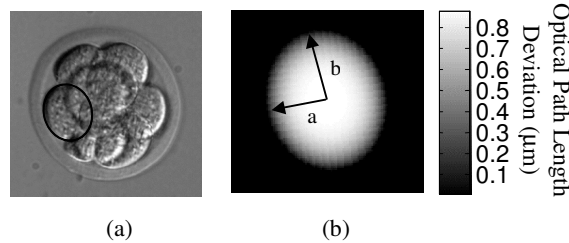


**Figure 5:** (a) Cell boundary created for chosen cell. (b) Ellipsoidal model cell of optical path length deviation created from the combination of the cell boundary with the optical path length deviation of a single cell.

Ellipsoidal equations were empirically analyzed to determine the best fit for cells within the OPD image. These equations included the equation for a parabolic ellipsoid:

$$\frac{x^2}{a^2} + \frac{y^2}{b^2} + \frac{z}{c} = 1, \quad (18)$$

the equation for a perfect ellipsoid:

$$\frac{x^2}{a^2} + \frac{y^2}{b^2} + \frac{z^2}{c^2} = 1, \quad (19)$$

the equation for a slightly flattened ellipsoid:

$$\left( \frac{x^2}{a^2} + \frac{y^2}{b^2} \right)^2 + \frac{z^2}{c^2} = 1, \quad (20)$$

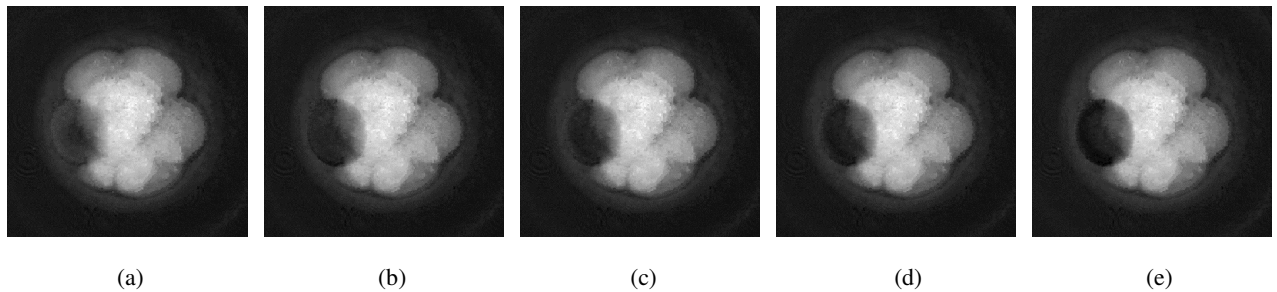
the equation for a flattened ellipsoid:

$$\left( \frac{x^2}{a^2} + \frac{y^2}{b^2} \right)^{\frac{5}{2}} + \frac{z^2}{c^2} = 1, \quad (21)$$

and the equation for a severely flattened ellipsoid:

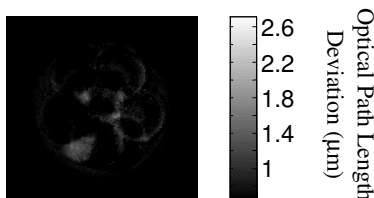
$$\left( \frac{x^2}{a^2} + \frac{y^2}{b^2} \right)^4 + \frac{z^2}{c^2} = 1. \quad (22)$$

Figure 6 shows the subtraction of model cells created by (18) – (22). The subtraction of (18) in Figure 6(a) shows some pixels within the subtracted area with an optical path length deviation greater than the zona pellucida. The subtraction of (19) in Figure 6(b) shows the pixels within the subtracted area having an optical path length deviation less than the maximum value corresponding to the zona pellucida but with a visible discontinuity at the boundary. The subtraction of (20) in Figure 6(c) also shows the pixels within the subtracted area having an optical path length deviation less than the maximum value corresponding to the zona pellucida but with a softer subtraction at the boundary. The subtraction of (21) in Figure 6(d) shows some pixels within the subtracted area that are equal to the optical path length deviation of the culture medium, which would signify that there is no contribution in optical path length deviation from the top and bottom portions of the zona pellucida. The subtraction of (22) in Figure 6(e) shows the pixel values that were equal to the optical path length deviation of the culture medium in Figure 6(d) are now less than the optical path length deviation of the culture medium, indicating too much optical path length deviation has been subtracted from the image. Equations (19) and (20) were chosen to be the best equations to create the model cell since the zona pellucida must have some optical path length deviation greater than the culture medium. Otherwise the optical path length deviation would either be constant or decreasing around the cells along the perimeter. Since the cells are pressed against each other and against the zona pellucida and do not have perfect ellipsoidal boundaries, equation (20) for a slightly flattened ellipsoid was chosen to create the model cells. However, this method could be completed with model cells created with (19) and that equation may be considered more appropriate in future experiments.



**Figure 6:** OPD image after subtraction of the model cell created by the equation for a (a) parabolic ellipsoid, (b) perfect ellipsoid, (c) slightly flattened ellipsoid, (d) flattened ellipsoid, and (e) severely flattened ellipsoid.

The model cell is subtracted from the OPD image revealing either the background culture medium and zona pellucida or additional cells hidden underneath. Elliptical boundaries are created for all cells visible in the DIC image and subtracted from the OPD image. Once all the visible cells have been accounted for, the subtracted OPD image is analyzed for hidden cells that could not be seen in the DIC image. Elliptical boundaries are fit to elliptically shaped regions or clusters with the approximate size of the cells previously subtracted in the OPD image. The approximate size takes into account the combination of the cross sectional area created by the previous cell boundaries and the total optical path length deviation of a single cell. Elliptical boundaries are fit to these regions and model cells are subtracted until no such regions remain and the count is complete as seen in Figure 7.



**Figure 7:** Final subtracted OQM image with the minimum of the colorbar value set to the minimum optical path length deviation of a single cell. A polar body remains in the bottom left portion, which is significantly smaller than the size of the previous cells selected in the DIC image.

A small region of optical path length deviation still exists in the lower left region of Figure 7, which corresponds to the polar body previously labeled in Figure 1. This region is considered a polar body and not a cell in this method because the boundary of the polar body is much smaller than the boundaries of the cells previously created within the DIC image. Observations of OQM images of live mouse embryos have shown variations of optical path length deviation associated with the polar bodies and thus more study is needed to define additional characteristics to differentiate the polar body from cells in the subtracted OPD image. Please see <http://www.keck3dfm.neu.edu/samplevideo> for a complete visualization of this cell counting method.

## 7. CELL COUNTING RESULTS

This cell counting method has been completed on 5 live mouse embryos. A z-stack of images was acquired with epi-fluorescence and analyzed to determine the ground truth number of cells. As previously mentioned, the number of nuclei corresponds to the exact number of cells. Single images were also acquired in the center focus plane of the embryo in DIC and OQM to count the number of cells with this method. These samples were used as a training set where the number of cells was known before this cell counting method was complete. This training set was used to determine the potential variation in cell sizes for embryos with different cell numbers since the cells divide asynchronously [35]. As seen in Table 1, accurate cell counts were obtained for the five samples once the correct cell boundaries were chosen.

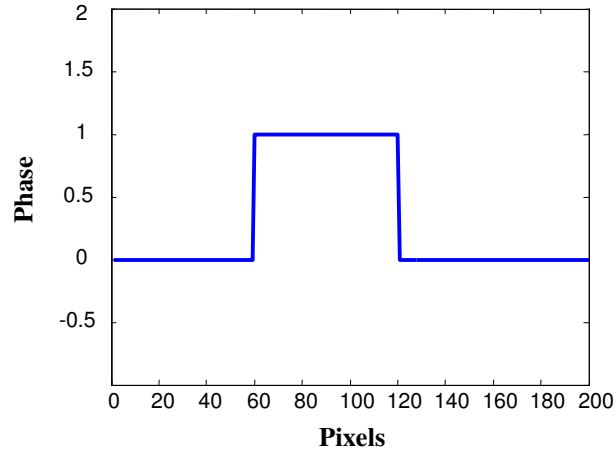
	<b>Epi-fluorescence Count</b>	<b>This Method</b>
1	13 cells	13 cells
2	14 cells	14 cells
3	16 cells	16 cells
4	17 cells	17 cells
5	25 cells	25 cells

**Table 1:** Results of cell counts produced by epi-fluorescence imaging of Hoechst stained nuclei and the method presented in this paper for a training set of five live mouse embryos. The number of cells was known before this cell counting method was completed.

We have reported a previous cell counting method using the OPD image alone, however the precision was less than desired for samples with a higher number of cells [36]. The results in this report show the power of utilizing both the DIC and OPD images for counting the number of cells in an embryo.

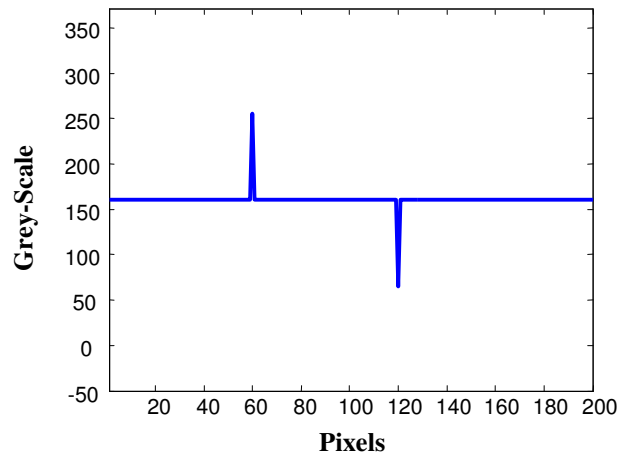
## 8. FUTURE WORK

This method is extremely accurate but it is a labor-intensive process. Additional work is required to either ease the selection of cell boundaries or automate the process. One idea is to combine two different DIC images of the embryo with a  $90^\circ$  rotation of the first polarizer in the path. The  $90^\circ$  rotation of the polarizer induces a sign reversal of the phase gradient across the image. This makes everything that was dark in the first DIC image light in the second DIC image and *vice versa*. Figure 8 shows an image of phase for an object with an increasing edge at pixel location 60 and a decreasing edge at pixel location 120.



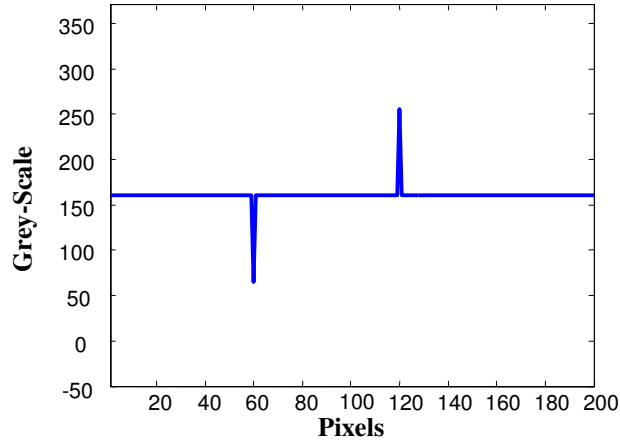
**Figure 8:** Phase image of an object with an increasing edge at pixel 60 and a decreasing edge at pixel 120.

Figure 9 shows a line going through the phase of Figure 8 in a DIC image (dic135 image) with light contrast representing increasing edge and dark contrast representing the decreasing edge.



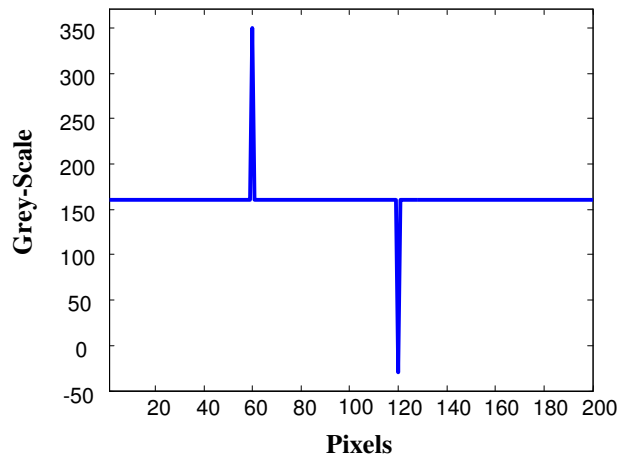
**Figure 9:** Plotted line of DIC image (dic135 image) for model edges with light contrast for increasing edge and dark contrast for decreasing edge going left to right.

Figure 10 shows the same line going through the phase image with the polarizer rotated  $90^\circ$  (dic45 image). The sign reversal of the phase gradient results in dark contrast for the increasing edge and light contrast for the decreasing edge.



**Figure 10:** Plotted line of DIC image with 90° rotation of polarizer (dic45 image).

Subtracting the dic45 image in Figure 10 from the dic135 image in Figure 9 results in a greater signal-to-noise ratio, and thus more contrast, for the edges seen in Figure 11. A constant grey-scale value of 160 was added to the subtraction to keep the plot in Figure 11 on the same axes as the previous figures. Therefore, subtracting the two DIC images of the embryo could help the user by providing clearer cell boundaries.



**Figure 11:** Plot of the subtraction of the dic45 image from the dic135 image (combined DIC image). A constant grey-scale value of 160 was added to the subtraction to aid in visualization of the concept.

Improvements should also be incorporated into the model to allow different total optical path length deviations that are dependent on the size of the cell. The assumption of each cell having the same optical path length deviation worked in this method because we were only looking for a total number of cells and not the analysis of remnant optical path length deviation in the final subtracted image. In reality, cells do not divide synchronously [35] and the method should be able to correct for varying cell sizes. Additional samples must also be analyzed with this method when the cell count is not known before the method is complete to show the true potential of the method.

## ACKNOWLEDGEMENTS

This work was supported in part by CenSSIS, the Center for Subsurface Sensing and Imaging Systems, under the Engineering Research Centers Program of the National Science Foundation (Award Number EEC-9986821).

## REFERENCES

- [1] CDC, "2002 Assisted Reproduction Technology Success Rates. National Summary and Fertility Clinic Reports," Atlanta, GA: US Department of Health and Human Services, CDC, 2004.
- [2] J. Martin, M. Park, "Trends in twin and triplet births: 1980-1997," *Natl. Vital Stat. Rep.*, **24**, pp. 1-16, 1999.
- [3] N.J. Sebire, "Swedish in vitro fertilization study," *Lancet*, **355**, pp. 845, 2000.
- [4] ESHRE Campus Course Report, "Prevention of twin pregnancies after IVF/ICSI by single embryo transfer," *Hum. Reprod.*, **16**, pp. 790-800, 2001.
- [5] O. Ozturk, S. Bhattacharya, A. Templeton, "Avoiding multiple pregnancies in art: Evaluation and implementation of new strategies," *Hum. Reprod.*, **16**, pp. 1319-1321, 2001.
- [6] D. De Neubourg, K. Mangelschots, E. Van Royen, M. Vercruyssen, G. Ryckaert M. Valkenburg, J. Barudy-Vasquez, J. Gerris, "Impact of patients' choice for single embryo transfer of a top quality embryo versus double embryo transfer in the first IVF/ICSI cycle," *Hum. Reprod.*, **17**, pp. 2621-2625, 2002.
- [7] J. Gerris, D. De Neubourg, K. Mangelschots, E. Van Royen, M. Vercruyssen, J. Barudy-Vasquez, M. Valkenburg, G. Ryckaert, "Elective single day 3 embryo transfer halves the twinning rate without decrease in the ongoing pregnancy rate of an IVF/ICSI programme," *Hum. Reprod.*, **17**, pp. 2626-2631, 2002.
- [8] R.M. Schultz, C.J. Williams, "The science of art," *Science*, **296**, pp. 2188-2190, 2002.
- [9] A.G. Sutcliffe, *IVF Children: The First Generation*. Parthenon Publishing, 2002.
- [10] B. Strömberg, G. Dahlquist, A. Ericson, O. Finnström, M. Köster, K. Stjernqvist, "Neurological sequelae in children born after in-vitro fertilisation: a population-based study," *Lancet*, **359**, pp. 461-465, 2002.
- [11] T. Gurgan, A. Demiroglu, "Why and how should multiple pregnancies be prevented in assisted reproduction treatment programmes?" *Reprod. Biomed. Online*, **9**, pp. 237-244, 2004.
- [12] J.M. Cummins, T.M. Breen, K.L. Harrison, J.M. Shaw, L.M. Wilson, J.F. Hennessey, "A formula for scoring human embryo growth rates in in vitro fertilization: Its value in predicting pregnancy and a comparison with visual estimates of embryo quality," *J. In Vitro Fertil. Embryo Transfer*, **3**, pp. 284-295, 1986.
- [13] F. Puissant, M. Van Rysselberge, P. Barlow, J. Deweze, F. Leroy, "Embryo scoring as a prognostic tool in ivf treatment," *Hum. Reprod.*, **2**, pp. 705-708, 1987.
- [14] V.N. Bolton, S.M. Hawes, C.T. Taylor, J.H. Parsons, "Development of spare human preimplantation embryos in vitro: An analysis of the correlations among gross morphology, cleavage rates, and development to blastocyst," *J. In Vitro Fertil. Embryo Transfer*, **6**, pp. 30-35, 1989.
- [15] D.S. Visser, F.R. Fourie, "The applicability of the cumulative embryo score system for embryo selection and quality control in an in-vitro fertilization/embryo transfer programme," *Hum. Reprod.*, **8**, pp. 1719-1722, 1993.
- [16] S. Ziebe, K. Petersen, S. Lindenberg, A.G. Andersen, A. Gabrielsen, A.N. Andersen, "Embryo morphology or cleavage stage: how to select the best embryos for transfer after in-vitro fertilization," *Hum. Reprod.*, **12**, pp. 1545-1549, 1997.
- [17] D.K. Gardner, W.B. Schoolcraft, "Culture and transfer of human blastocysts," *Curr. Opin. Obstet. Gynecol.*, **11**, pp. 307-311, 1999.
- [18] J. Tesarik, E. Greco, "The probability of abnormal preimplantation development can be predicted by a single static observation on pronuclear stage morphology," *Hum. Reprod.*, **14**, pp. 1318-1323, 1999.
- [19] N. Desai, J. Goldstein, D. Rowland, J. Goldfarb, "Morphological evaluation of human embryos and derivation of an embryo quality scoring system specific for day 3 embryos: a preliminary study," *Hum. Reprod.*, **15**, pp. 2190-2196, 2000.
- [20] C. Racowsky, K.V. Jackson, N.A. Cekleniak, J.H. Fox, M.D. Hornstein, E.S. Ginsburg, "The number of eight-cell embryos is a key determinant for selecting day 3 or day 5 transfer," *Fertil. Steril.*, **73**, pp. 558-564, 2000.
- [21] L. Scott, R. Alvero, M. Leondires, B. Miller, "The morphology of human pronuclear embryos is positively related to blastocyst development and implantation," *Hum. Reprod.*, **15**, pp. 2394-2403, 2000.
- [22] C.M. Warner, C.A. Brenner, "Genetic regulation of preimplantation embryo survival," *Current Topics in Developmental Biology*, **52**, pp. 151-192, 2001.
- [23] G. De Placido, M. Wilding, I. Strina, E. Alviggi, C. Alviggi, A. Mollo, M.T. Varicchio, A. Tolino, C. Schiattarella, B. Dale, "High outcome predictability after ivf using a combined score for zygote and embryo morphology and growth rate," *Hum. Reprod.*, **17**, pp. 2402-2409, 2002.
- [24] C.M. Warner, J.A. Newmark, M. Comiskey, S.R. De Fazio, D.M. O'Malley, M. Rajadhyaksha, D.J. Townsend, S. McKnight, B. Roysam, P.J. Dwyer, C.A. DiMarzio, "Genetics and imaging to assess oocyte and preimplantation embryo health," *Reprod. Fertil. Develop.*, **16**, pp. 729-741, 2004.

- [25] I. Agerholm, "Embryo registration versus embryo scoring - the experience from a whole nation using the same system," *ESHRE Campus Symposium*, Copenhagen, Denmark, 2005.
- [26] U. Eichenlaub-Ritter, "The polscope as an analytical tool," *ESHRE Campus Symposium*, Copenhagen, Denmark, 2005.
- [27] M.L. Grohndahl, "Present and future approaches for oocyte and zygote quality assessment," *ESHRE Campus Symposium*, Copenhagen, Denmark, 2005.
- [28] C. Hnida, I. Agerholm, S. Ziebe, "Traditional detection versus computer-controlled multilevel analysis of nuclear structures from donated human embryos," *ESHRE Campus Symposium*, Copenhagen, Denmark, 2005.
- [29] C. Hnida, E. Engenheiro, S. Ziebe, "Computer-controlled, multilevel, morphometric analysis of blastomere size as biomarker of fragmentation and multinuclearity in human embryos," *ESHRE Campus Symposium, Copenhagen*, Denmark, 2005.
- [30] K. Lundin, "Morphological markers of embryo quality," *ESHRE Campus Symposium*, Copenhagen, Denmark, 2005.
- [31] D. Gardner, M. Lane, "Culture and selection of viable blastocysts: a feasible proposition for human IVF?" *Hum. Reprod.*, **3**, pp. 367-382, 1997.
- [32] D.O. Hogenboom, C.A. DiMarzio, T.J. Gaudette, A.J. Devaney, S.C. Lindberg, "Three-dimensional images generated by quadrature interferometry," *Optics Letters*, **23**, pp. 783-785, 1998.
- [33] J.A. Newmark, W.C. Warger II, C.C. Chang, G.E. Herrera, D.H. Brooks, C.A. DiMarzio, C.M. Warner, "Determination of the number of cells in preimplantation embryos by using non-invasive optical quadrature microscopy in conjunction with differential interference contrast microscopy," unpublished.
- [34] D.J. Townsend, K.D. Quarles, A.L. Thomas, W.S. Rockward, C.M. Warner, J.A. Newmark, C.A. DiMarzio, "Quantitative phase measurements using a quadrature tomographic microscope," *Proc. of SPIE*, **4964**, pp. 59-65, 2003.
- [35] K.A. Rafferty, Jr., *Methods in Experimental Embryology of the Mouse*. Baltimore, MD: John Hopkins University Press, 1970, pp. 82.
- [36] W.C. Warger II, J.A. Newmark, C.C. Chang, D.A. Brooks, C.M. Warner, C.A. DiMarzio, "Combining optical quadrature and differential interference contrast to facilitate embryonic cell counts with fluorescence imaging for confirmation," *Proc. SPIE*, **5699**, pp. 334-341, 2005.

\*wwarger@ece.neu.edu, Ph: 617 373 8570, Fax: 617 373 7783